VOLUME 52 JOURNAL OF PHYSICAL OCEANOGRAPHY APRIL 2022

Oceanic Advection Controls Mesoscale Mixed Layer Heat Budget and Air–Sea Heat Exchange in the Southern Ocean

YU GAO,[a] IGOR KAMENKOVICH,[a] NATALIE PERLIN,[b,a] AND BENJAMIN KIRTMAN[b,a]

[a] *Rosenstiel School of Marine and Atmospheric Sciences, University of Miami, Miami, Florida*
[b] *Cooperative Institute for Marine and Atmospheric Studies, University of Miami, Miami, Florida*

(Manuscript received 18 March 2021, in final form 20 December 2021)

ABSTRACT: We analyze the role of mesoscale heat advection in a mixed layer (ML) heat budget, using a regional high-resolution coupled model with realistic atmospheric forcing and an idealized ocean component. The model represents two regions in the Southern Ocean, one with strong ocean currents and the other with weak ocean currents. We conclude that heat advection by oceanic currents creates mesoscale anomalies in sea surface temperature (SST), while the atmospheric turbulent heat fluxes dampen these SST anomalies. This relationship depends on the spatial scale, the strength of the currents, and the mixed layer depth (MLD). At the oceanic mesoscale, there is a positive correlation between the advection and SST anomalies, especially when the currents are strong overall. For large-scale zonal anomalies, the ML-integrated advection determines the heating/cooling of the ML, while the SST anomalies tend to be larger in size than the advection and the spatial correlation between these two fields is weak. The effects of atmospheric forcing on the ocean are modulated by the MLD variability. The significance of Ekman advection and diabatic heating is secondary to geostrophic advection except in summer when the MLD is shallow. This study links heat advection, SST anomalies, and air–sea heat fluxes at ocean mesoscales, and emphasizes the overall dominance of intrinsic oceanic variability in mesoscale air–sea heat exchange in the Southern Ocean.

KEYWORDS: Southern Ocean; Mesoscale processes; Atmosphere-ocean interaction; Heat budgets/fluxes; Coupled models

1. Introduction

An important question in atmosphere–ocean interaction is how the ocean dynamics, rather than the atmosphere, drive the variability in the sea surface temperature (SST) and air–sea heat exchange. This study characterizes the regime in which oceanic heat advection dominates the mixed layer (ML) heat budget and induces SST anomalies in a semi-idealized framework in the Southern Ocean. The induced SST anomalies subsequently lead to thermal damping by the atmosphere through air–sea heat flux exchange (Liu et al. 1994; Okumura et al. 2001; Small et al. 2008; Kirtman et al. 2012; Bishop et al. 2017; Small et al. 2019). These air–sea heat exchange processes are thus directly linked to oceanic heat advection. This regime corresponds to oceanic mesoscales, which are spatial scales of tens to hundreds of kilometers. Scale at which SST variability transitions from the ocean- to atmosphere-driven regime was found to be around 500 km in Antarctic Circumpolar Current (ACC) region (Bishop et al. 2017; Laurindo et al. 2019; Small et al. 2019). Ma et al. (2016) and Bishop et al. (2020) discussed a thermal damping effect by ocean-driven heat fluxes and demonstrated that underestimating mesoscale air–sea feedback could lead to considerable bias in climate simulations. Since highly variant ML depth (MLD) in the Southern Ocean modulates thermal inertia of the upper ocean, one could expect the MLD to modulate dominant processes in the heat budget as well.

We focus on the Southern Ocean because of its strong currents, strong mesoscale variability, and highly variant MLD. The Southern Ocean has prominent meridional gradients and mostly zonal fronts and currents that extend to considerable depths (Orsi et al. 1995). Mesoscale variability experiences notable changes in zonal direction as well. Mesoscale currents are strong east of the Agulhas region and weak in the Pacific sector. For example, Sallee et al. (2008) showed that eddy diffusivity computed from surface drifters and satellite altimetry observations in the Southern Ocean, peaks in the Agulhas Retroflection current north of the ACC. Therefore, one can expect mesoscale air–sea heat exchange to be stronger in the Indian sector compared to the Pacific sector.

This study links SST anomalies and air–sea heat exchange to three-dimensional heat advection at the ocean mesoscales, while previous efforts have mostly focused on the role of advection in the heat budget. Although thermal advection can play an essential role in the upper-ocean heat budget (Roberts et al. 2017; Small et al. 2020), its relation to SST variability is not easily determined because of competing contributions from the winds, air–sea heat exchanges and variability of the MLD. Previous studies of upper-ocean heat budget analysis primarily addressed how the oceanic heat advection, as opposed to atmospheric forcing, that drives the SST tendencies in the North Atlantic region (Buckley et al. 2014, 2015), the California Current System (Seo et al. 2016), and the Gulf of Mexico (Putrasahan et al. 2017). A direct link between mesoscale oceanic heat advection and SST anomalies, however, has not been established yet. A notable

---

Denotes content that is immediately available upon publication as open access.

Corresponding author: Yu Gao, ygao@rsmas.miami.edu

DOI: 10.1175/JPO-D-21-0063.1

difference between the previous studies is that advection is defined as the 3D convergence of ocean heat flux in the present study, while only its horizontal (lateral) component is commonly accounted for in earlier works (Vivier et al. 2010; Seo et al. 2016; Putrasahan et al. 2017). For example, Vivier et al. (2010) found that anomalous surface heat flux is the dominant term in most of the Southern Ocean, while lateral geostrophic heat fluxes derived from altimetry are a major contributor in the main ACC pathways. Faure et al. (2011) analyzed surface mixed layer heat budget south of Africa using various observational datasets; they found that heat is mainly transported via lateral geostrophic advection of the Agulhas Current. Putrasahan et al. (2017) demonstrated that lateral oceanic mesoscale heat advection supports warm SST anomalies in the Gulf of Mexico. Cronin et al. (2013) used surface mooring data in the recirculation gyre south of the Kuroshio Extension region, and analyzed balance of processes affecting the upper-ocean heat content and temperature variations in the surface mixed layer. They derived an upper-ocean heat budget for a time-varying MLD and found that surface heat loss is replenished through the horizontal heat advection during winter.

Finally, previous studies primarily looked into the upper-ocean heat balance in the Southern Ocean assuming fixed MLD, instead of varying MLD used in this study. Earlier studies, therefore, did not account for the role of MLD in heat budget analyses, despite upper-ocean heat inertia being closely related to MLD. In a study based on data-assimilating Southern Ocean State Estimate (Mazloff et al. 2010), Tamsitt et al. (2016) examined the 3D oceanic heat advection integrated over the upper 614 m in the Southern Ocean and concluded that the principal time-mean heat balance is between the air–sea heat flux and heat advection. They found that in the Agulhas Return Current region, the convergence of geostrophic and vertical advective fluxes is balanced mainly by ocean heat loss. Small et al. (2020) showed that 3D oceanic heat advection dominates the upper-ocean heat budget on monthly time scales. Their study attributed most of the upper-ocean heat content tendency to heat advection, while the role of the wind-driven Ekman heat advection is found secondary. The relative importance of the advection term increases rapidly with depth, and the 400-m heat budget in their study is entirely dominated by advection.

The MLD changes dramatically with time and space in the Southern Ocean, especially in the vicinity of the Subantarctic Front. Our study establishes how the MLD modulates the role of heat advection in the heat budget and how it affects the SST variability at mesoscales. Although some past studies looked into how the MLD affects the SST variability in the Southern Ocean, they focused on larger scales and did not address the importance of oceanic advection at the mesoscales. For example, Tozuka and Cronin (2014) found that in the Southern Ocean, the large-scale SST is more sensitive to diabatic heating where the MLD is shallower. The MLD variation can therefore modulate the strength of SST fronts such that diabatic heating is amplified where the mixed layer is shallow and weakened where the mixed layer is deep. Tozuka et al. (2018) also quantified relative importance of diabatic heating and MLD in large-scale horizontal SST variations. An observation-based assessment of the Southern Ocean mixed-layer heat budget (Dong et al. 2007) pointed out that the large-scale geostrophic advection plays a small role in comparison to the meridional Ekman heat advection. However, their assessment had a substantial imbalance in the regional heat budget due to data limitations.

To sum up, we aim to answer the following three questions using an improved ML heat budget analysis:

1) What is the role of mesoscale advection in warming/cooling of the ML, in generating SST anomalies, and driving air–sea heat exchanges?
2) How does the MLD affect the relative importance of oceanic heat advection in the ML heat balance, compared to the atmospheric forcing?
3) How do the relations in 1 and 2 depend on spatial scales of oceanic processes and the strength of ocean currents?

The paper is organized as follows: the next section discusses the methodology, including the Regional Ocean–Atmosphere Model (ROAM), ML heat budget, and definitions of large-scale and mesoscale oceanic anomalies. Further, we examine how the MLD and ocean currents speed influences the relative importance of oceanic heat advection compared to diabatic heating. Most importantly, we analyze how the heat advection affects the mesoscale heating/cooling and SST anomalies. Finally, we will discuss the relative importance of Ekman heat advection in order to determine whether the ML heat budget and SST anomalies are driven by atmospheric variability or intrinsic oceanic processes. Study conclusions are presented and discussed in the last section.

2. Methodology

a. Regional Ocean–Atmosphere Model

We use the high-resolution fully coupled ROAM with an idealized ocean component and realistic atmospheric forcing. The modeling system and simulations analyzed in this study are described in detail in Perlin et al. (2020), and we provide only a brief description here. This semi-idealized model is built for studies of the air–sea interaction and upper-ocean dynamics in portions of the Southern Ocean. The atmospheric component of the model is the U.S. Navy Ocean–Atmosphere Mesoscale Prediction System (Hodur 1997), forced by lateral boundary conditions from the global reanalysis dataset. This dataset is 6-hourly 0.25° global NCEP FNL analysis and Global Forecast System (GFS). The atmospheric component of the coupled model has two nested domains: the inner domain that is fully coupled with the ocean component, and the outer domain that is forced with daily SST product. Daily SST fields come from the National Oceanic and Atmospheric Administration (NOAA) version 2 daily optimum interpolation (OI) analyses on a 0.25° grid (Reynolds et al. 2007), and are used as lower boundary conditions for the outer grid. The outer atmospheric domain has 27-km resolution (i.e., grid box size), while the inner atmospheric domain that coupled with the ocean component has 9-km horizontal resolution. Both

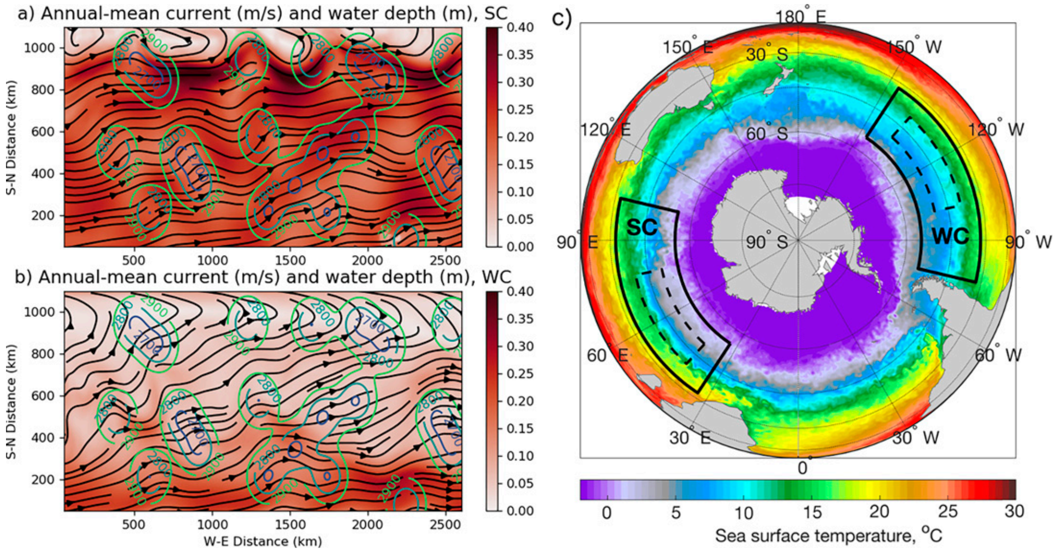
a) Annual-mean current (m/s) and water depth (m), SC

b) Annual-mean current (m/s) and water depth (m), WC

c)

FIG. 1. (a),(b) Annual mean current speed (shading), velocity (vectors) and water depth (contours) in 2016 as marked. Maximum water depth is 3000 m; depth contours indicate 25 randomized Gaussian-shaped seamounts. (c) Geographical location of SC and WC model domains. Solid black contours outline the outer 9-km atmospheric grids, and dashed contours show the corresponding ocean grid domains.

domains have 49 vertical layers. The atmospheric component uses one-way nesting approach with no feedback from the inner domain to the outer one. To smooth the transition between the two types of SST sources, the inner domain employs a blending scheme that ensures a gradual transition between the ROMS-simulated and observed SST values over 100-km region surrounding the ocean grid.

The ocean component is the Regional Ocean Modeling System (Shchepetkin and McWilliams 2005), forced at the surface by net heat, solar, and momentum fluxes from the atmospheric component and restoring boundary conditions for salinity. The spatial resolution is 2.5 km in both zonal and meridional direction, and 30 sigma layers in the vertical direction stretching from the surface to the bottom. The spatial resolution in the ocean component is sufficient to fully resolve variability at the first baroclinic Rossby deformation radius. Therefore, the oceanic mesoscale variability and air–sea coupling can be fully resolved in the ocean component. The oceanic domain is a zonally reentrant channel 2800 km long in the zonal direction and 1120 km wide in the meridional direction. Maximum depth of the channel is 3000 m. This ocean domain is fully coupled to the inner atmospheric domain. Twenty-five randomized Gaussian-shaped seamounts are added to the floor in order to keep the net zonal transport close to reasonable values (Pennel and Kamenkovich 2014), which is shown in Fig. 1. The sponge layers at the southern and northern channel walls are used to keep the large-scale meridional temperature and salinity gradients close to the prescribed values, which are derived from observations.

To ensure a smooth transition between SST in the outer and inner atmospheric domains, the model coupling software blends them within an additional domain with the 2.5-km spatial resolution (equivalent to the ocean grid spacing). This domain extends 40 grid points beyond the ocean grid, i.e., 100 km outward. The blending scheme combines the two SST fields and gives progressively higher weights, from 0 to 1, to the satellite OI SST and lower weights to the modeled SST as one moves away from the inner region. This blended SST product is then interpolated into the nested atmospheric model grid using the coupler software regridding capability.

ROAM is formulated in two domains with distinct oceanic regimes: the Strong Current (SC) case with faster ocean currents (Fig. 1a), larger meridional temperature gradient and higher eddy kinetic energy (EKE), and the Weak Current (WC) case with slower currents (Fig. 1b), smaller meridional temperature gradient and lower EKE. The SC and WC cases use lateral boundary conditions in the atmospheric and oceanic domains that are derived from two separate geographical locations in the Southern Hemisphere, which corresponds to two distinct oceanic regimes: the Western Indian sector for the SC case, and the Eastern Pacific sector for the WC case (Fig. 1c). The corresponding ocean domain in the SC and WC regions are in the same latitude band (40°–50°S). The longitude band of the SC ocean domain ranges from 42.2° to 77.9°E. The longitude band of the WC ocean domain ranges from 102.1° to 137.8°W. The ocean model employs a Cartesian grid, but latitude/longitude coordinates are used in the coupler software for regridding purposes. The coupled model had been spun up for 2 years, following a spinup of the ocean-only model for 12 and 24.5 years in the SC and WC cases, respectively. This time is deemed to be sufficient for the equilibration of the upper-ocean measured by domain-average eddy kinetic energy. Two-year simulations of both cases were carried out after the spinups, starting at 0000 UTC on 24 July 2015 and ending at 0000 UTC 28 July 2017. We are particularly interested in mesoscale and subseasonal variability so the analysis in this study is based on monthly averages.

Perlin et al. (2020) showed that the time- and zonal-mean isopycnals are steeper in the SC case compared to the WC case, and this difference in the large-scale stratification leads to stronger zonal currents and mesoscale activity in the SC case (Fig. 1). The annual-mean meridional SST gradient is about 0.9° and 0.5°C (100 km)$^{-1}$ in the SC and WC case, respectively. The annual-mean net volume transport is approximately 140 and 40 Sv (1 Sv ≡ 10^6 m^3 s^{-1}) in the SC and WC case, respectively. In a broad agreement with climatological data, the model winds are predominantly westerly in both regions. The annual-mean current speed is 0.19 and 0.08 m s^{-1} in the SC and WC cases, respectively. The annual-mean EKE is 0.024 and 0.015 m^2 s^{-2} in the SC and WC case, respectively. Moreover, Perlin et al. (2020) validated that the wind–SST coupling coefficients in the SC and WC cases are in agreement with the earlier estimates in O'Neill et al. (2012) and Perlin et al. (2014), which confirms that the modeled atmospheric response to SST anomalies in our studies is realistic.

The semi-idealized setting facilitates detailed analysis of the ML heat budget and a meaningful comparison of the SC and WC cases. The high spatial resolution (2.5 km) used here cannot be afforded by global climate models, and the advantage of this regional study is the full resolution of the oceanic mesoscale. The reentrant channel configuration avoids the need for open boundary conditions in these regional simulations. At the same time, there are several shortcomings that include the following: 1) periodic zonal boundary conditions are likely the main reason for the mean currents in the SC case to be weaker than those observed in the real Southern Ocean sector of the Indian Ocean (see Perlin et al. 2020); 2) idealized topography cannot produce realistic topographic effects, particularly in the SC case, because idealized topography cannot represent all effects of the real topography in the Southern Ocean; and 3) potential distortion of zonally propagating atmospheric anomalies as they propagate from the outer to the inner domain at the east and west boundaries of oceanic domain.

b. Ocean mixed layer heat budget

In the Southern Ocean, the density-based criterion was chosen to define the ocean MLD because of the density-compensating nature of temperature and salinity variability in this region (Sallée et al. 2006; Dong et al. 2007; Li and Lee 2017). The MLD is defined as the depth at which the potential density increases by 0.03 kg m^{-3} relative to sea surface density. The depth-dependent heat budget of the ocean can be expressed as below:

$$\rho_0 C_p \frac{\partial \theta}{\partial t} = \frac{\partial d}{\partial z} - \rho_0 C_p \mathbf{u} \cdot \nabla \theta - \rho_0 C_p \nabla \cdot (\kappa_h \nabla \theta) + \rho_0 C_p \frac{\partial}{\partial z}\left[\kappa_z \left(\frac{\partial \theta}{\partial z}\right)\right], \tag{1}$$

with boundary condition

$$q|_{z=0} = Q_{\text{net}}, \tag{2}$$

where θ is the potential temperature, ρ_0 is the density of seawater, C_p is the specific heat of seawater, q is the net downward heat flux (positive into the ocean) that changes with depth, $u = (u, v, w)$ is the three-dimensional velocity vector, and κ_h and κ_z are the horizontal and vertical diffusion coefficients, respectively. The Q_{net} is the downward net heat flux at the surface, which consists of four components:

$$Q_{\text{net}} = Q_{\text{SW}} + Q_{\text{LW}} + Q_s + Q_l, \tag{3}$$

where Q_{SW} is the shortwave heat flux, Q_{LW} is the longwave heat flux, Q_s is the sensible heat flux, and Q_l is the latent heat flux. The sign is positive when the surface heat flux is downward throughout this paper.

To examine the ML heat budget, we take the integral of Eq. (1) over the ocean MLD, H, yielding

$$\underbrace{\int_{-H}^{0} \rho_0 C_p \frac{\partial \theta}{\partial t}\, dz}_{\text{ML heating/cooling}} = \underbrace{Q_{\text{net}} - q_H}_{\text{ML diabatic heating}} \underbrace{- \rho_0 C_p \int_{-H}^{0} \mathbf{u} \cdot \nabla \theta\, dz}_{\text{ML-integrated advection}} + \underbrace{\rho_0 C_p \int_{-H}^{0} \left[\nabla \cdot (\kappa_h \nabla \theta) + \frac{\partial}{\partial z} \kappa_z \left(\frac{\partial \theta}{\partial z}\right)\right] dz}_{\text{ML-integrated diffusion}} \tag{4}$$

where the ML heating/cooling term can be further split into two terms: the entrainment and ML heat content tendency, which tend to balance each other according to our analysis. Since our focus is on the relative importance of the oceanic heat advection, we choose to analyze the heating/cooling term as shown in (4). We calculate the each term in ML heat budget with 6-hourly model data output in offline diagnostics. A quantity of q_H is the downward shortwave radiation at the MLD. According to Paulson and Simpson (1977),

$$q_H = q_0 \left[R \exp\left(\frac{H}{\gamma_1}\right) + (1 - R) \exp\left(\frac{H}{\gamma_2}\right)\right], \tag{5}$$

where H is the MLD, $R = 0.58$ is a separation constant, and $\gamma_1 = 0.35$ m and $\gamma_2 = 23.0$ m are attenuation length scales in clear water. All the heat budget terms are explicitly derived from 6-hourly output with offline diagnostics.

c. Definition of anomalies

To explore the scale dependence in the air–sea coupling, we define the velocity $\mathbf{u}^*$ and temperature θ^* anomalies as deviations from the low-pass spatially filtered fields, $[\mathbf{u}]$ and temperature $[\theta]$:

$$\mathbf{u}^* = \mathbf{u} - [\mathbf{u}] \tag{6}$$

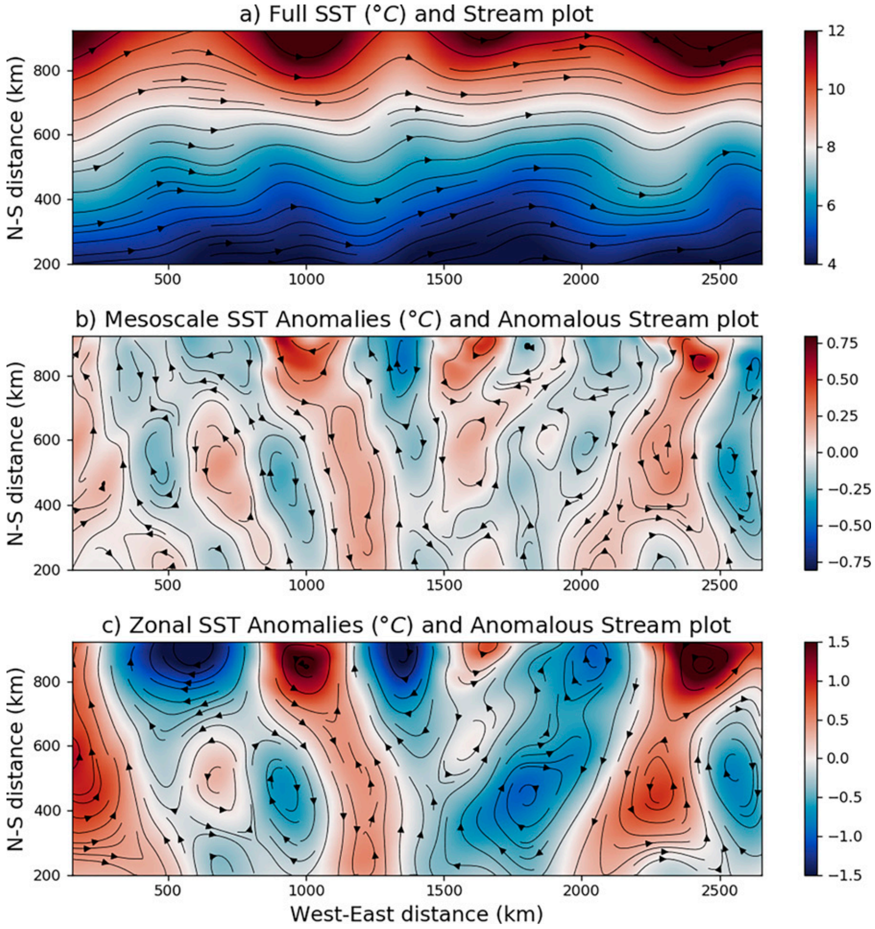

FIG. 2. (a) Full SST field (shading) and stream plots of surface currents (vectors), (b) mesoscale, and (c) zonal SST anomalies (shading) and stream plots of spatial anomalies of surface currents (vectors). All fields are time averaged in the SC case in August 2016.

and

$$\theta^* = \theta - [\theta]. \tag{7}$$

Two choices for the spatial filter are used in this study: 1) a zonal average and 2) a running mean smoothing with a 300 km × 300 km square filter. We refer to the departures from the zonal-mean as zonal anomalies, which are dominated by large-scale features and include stationary meanders (Fig. 2c). We refer to the departures from the 300-km box average as mesoscale anomalies (Fig. 2b). In this study, we apply these two different filters separately as follows:

$$\mathbf{u}^*_{\mathrm{mesoscale}} = \mathbf{u} - [\mathbf{u}]_{\mathrm{300km\text{-}average}} \tag{8}$$

$$\theta^*_{\mathrm{mesoscale}} = \theta - [\theta]_{\mathrm{300km\text{-}average}} \tag{9}$$

and

$$\mathbf{u}^*_{\mathrm{zonal}} = \mathbf{u} - [\mathbf{u}]_{\mathrm{zonal\text{-}average}} \tag{10}$$

$$\theta^*_{\mathrm{zoanl}} = \theta - [\theta]_{\mathrm{zonal\text{-}average}}. \tag{11}$$

Our spectra analysis (not shown) indicates that a 300-km highpass filtering effectively removes scales longer than approximately 200 km, which we consider a reasonable cutoff scale for the mesoscales at these latitudes. For example, according to linear stability theories, the most unstable wavelength is several Rossby deformation radii (Vallis 2006). We estimated the first baroclinic Rossby deformation radius using the following expression:

$$L_{R,n} = \frac{ND}{n\pi f}, \tag{12}$$

where $n = 1$, N is the buoyancy frequency, D is the water depth, and f is Coriolis frequency. We used domain- and time-mean N and H values to estimate first baroclinic Rossby deformation radii, which are 26 and 37 km in SC and WC case, respectively. These estimates are consistent with the calculations by Chelton et al. (1998) for the corresponding latitudes in the Southern Ocean. Note that the zonal-mean filter yields a two-dimensional (depth-meridional) large-scale anomalies, while the 300-km filter yields three-dimensional large-scale anomalies.

The advection term in (4) can be further decomposed as follows:

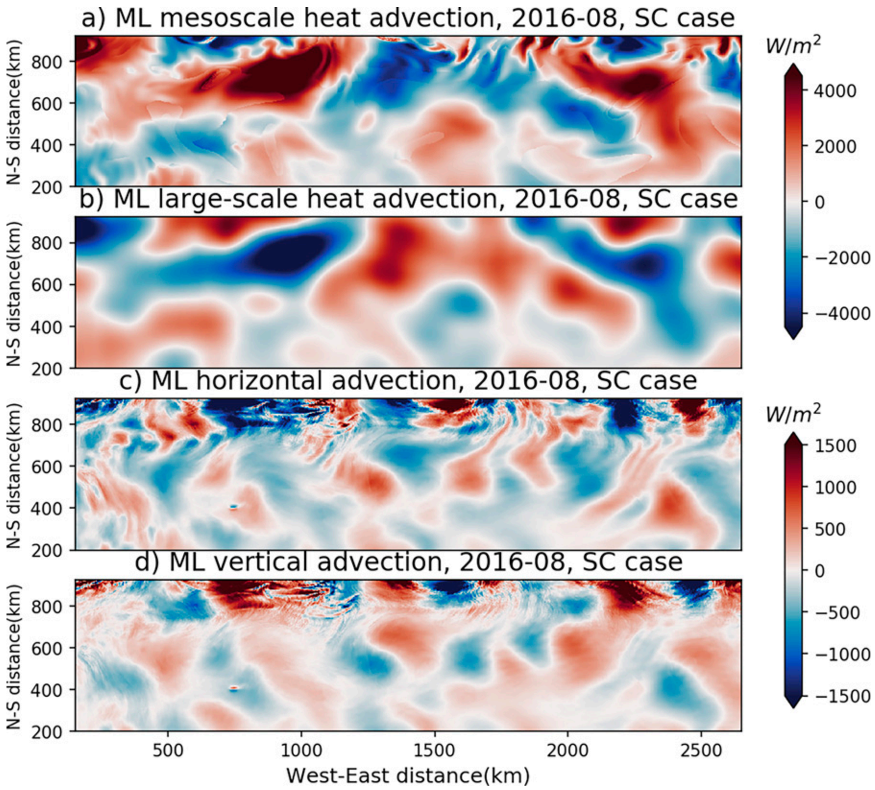

FIG. 3. (a) ML-integrated mesoscale heat advection in the SC case, (b) ML-integrated large-scale heat advection in the SC case, (c) ML-integrated horizontal/lateral advection in the SC case, and (d) ML-integrated vertical advection in the SC case. All fields are monthly averages for August 2016.

$$\underbrace{-\rho_0 C_p \int_{-H}^{0} \mathbf{u}\cdot\nabla\theta\, dz}_{\text{total advection}} = \underbrace{-\rho_0 C_p \int_{-H}^{0} [\mathbf{u}]\cdot\nabla[\theta] dz}_{\text{large-scale advection}} \underbrace{- \rho_0 C_p \int_{-H}^{0} \left([\mathbf{u}]\cdot\nabla\theta^{*} + \mathbf{u}^{*}\cdot\nabla[\theta] + \mathbf{u}^{*}\cdot\nabla\theta^{*}\right) dz}_{\text{mesoscale advection}}. \tag{13}$$

To identify the processes responsible for ML heating/cooling, we further decomposed the ML heating/cooling terms into two parts, using the same two filtering methods:

$$\underbrace{\int_{-H}^{0} \rho_0 C_p \frac{\partial\theta}{\partial t}\, dz}_{\text{ML heating/cooling}} = \int_{-H}^{0} \rho_0 C_p \frac{\partial[\theta]}{\partial t}\, dz + \int_{-H}^{0} \rho_0 C_p \frac{\partial\theta^{*}}{\partial t}\, dz. \tag{14}$$

This decomposition uses explicit spatial-scale dependence and is arguably more applicable for parameterizing of mesoscales in climate models than the decomposition based on time averaging. Note that all terms in Eqs. (13) and (14) are integrated over the full (unfiltered) MLD.

Figure 2 shows an example of the full SST field and SST anomalies estimated using two different filters in the SC case. Zonal SST anomalies are larger in magnitudes and size than mesoscale SST anomalies. Stream plots in Figs. 2b and 2c demonstrate that both mesoscale surface currents and zonal anomalies are consistent with the geostrophic dynamics. This consistency indicates that anomalies in Ekman currents are weaker than geostrophic anomalies. Despite high spatial resolution that technically permits submesoscale dynamics in this study, the ratio between relative vorticity and the Coriolis parameter is found to be small. Note that Figs. 2 and 3 show only the inner region of the ocean domain, 200 km away from the northern and southern boundaries, which minimizes the direct influence of the sponge boundaries.

Most of the analysis in the subsequent sections is based on monthly averages of various terms in the heat balance. Other averaging periods have been considered and tested as well, such as 10 days, 20 days, 2 months, and 3 months for both mesoscale and zonal anomalies in the heat budget calculations. We comment on the differences when necessary.

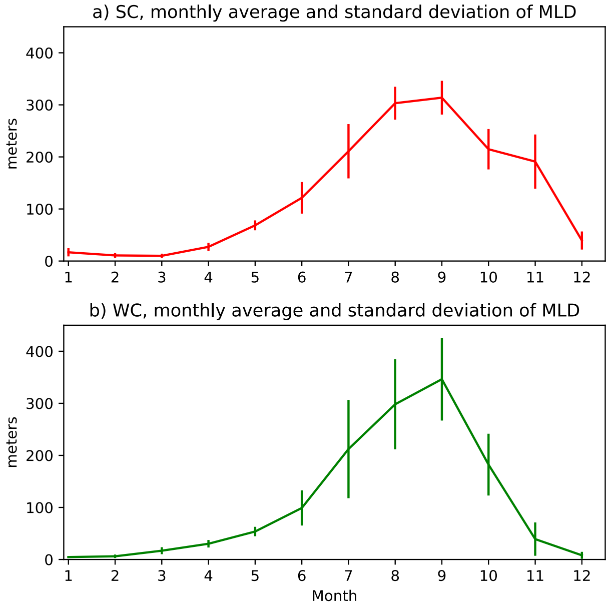

FIG. 4. Time series of the monthly domain average and standard deviation of MLD in the (a) SC case and (b) WC case.

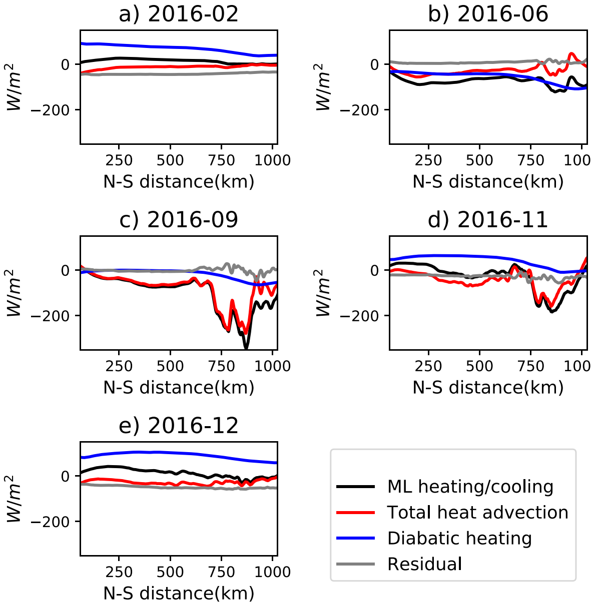

FIG. 5. Zonal-mean and monthly mean ML heat budget terms (W m^{-2}) in the SC case: ML heating/cooling term, ML heat advection term, diabatic heating term, and the residual term. The residual term includes heat diffusion at the base of the ML, lateral diffusion of heat and numerical errors. The legend is shown at the lower right corner. Average uncertainty, measured by standard error of the mean (SEM), in ML heating/cooling is 2.86 W m^{-2}. Average uncertainty in heat advection is 4.44 W m^{-2}. Average uncertainty in surface heat flux is 0.43 W m^{-2}. Average uncertainty in residual is 2.21 W m^{-2}.

Decomposition of large-scale and mesoscale heat advection estimated using the 300-km box high-pass filter demonstrates that mesoscale (eddy) components are comparable to those of large scales (mean) (Figs. 3a,b). Similarly, Tamsitt et al. (2016) found eddy components of the geostrophic advection to be of a similar magnitude as the mean geostrophic advection, in particular, in regions with high eddy variability, such as the western boundary currents and ACC. Our results are, therefore, in qualitative agreement with their study. Furthermore, Tamsitt et al. (2016) found that, due to cancellation of the mean and eddy components of the vertical heat fluxes, the net contribution of the vertical advection into the heat budget is small as compared to the horizontal terms. In contrast, we found that the ML-integrated vertical heat advection is of similar magnitude to the horizontal terms, and the horizontal and vertical components are of the opposite signs (Figs. 3c,d). This discrepancy between the two studies is likely explained by the differences in MLD estimation: a varying MLD is used for the integrated heat budget in our study, whereas Tamsitt et al. (2016) used a much deeper fixed ML depth (614 m), where the vertical fluxes can be expected to be small.

3. Results

a. ML heat balance

1) SEASONALITY OF THE ZONAL-MEAN HEAT BUDGET

Consistent with earlier estimates in the Southern Ocean (Dong et al. 2008; Sallée et al. 2010), the MLD in ROAM simulations exhibits strong seasonal variability. Monthly and domain-averaged MLD varies from tens of meters in summer to hundreds of meters in winter (Fig. 4). The MLD reaches its maximum in September and minimum in January–February (Fig. 4). As a result of this MLD variability, considerable seasonal changes were also found in the ML heat budget. The zonal-mean ML heat budget discussed here is computed by zonally averaging the Eq. (4). This analysis can give us insights into the large-scale heat budget and its seasonality. The MLD is shallow during the austral summer months (December–February), and little meridional structure is seen in the zonal average of each term in the ML heat balance equation in the SC case (Fig. 5a). The diabatic heating term in Eq. (4) is dominant in the heat budget in summer; ML-integrated advection term is smaller at this time because of the shallow ML. Advection acts to cool the ML, counteracting the overall warming driven by the diabatic term. The residual term, which includes heat diffusion at the base of the ML, lateral diffusion of heat, and numerical errors, is relatively large in this time period. Numerical errors in the residual term appear from discretization of the heat budget equation, as well as from the interpolation in the integration over MLD and integration in time. These numerical errors are expected to be small compared to the vertical diffusion. A relatively large residual term implies that the vertical diffusion is more important in summer than in winter, which is explained by sharper vertical gradients in temperature.

As the ML starts to deepen in April, the relative importance of diabatic heating decreases. The advection term becomes comparable to the diabatic cooling in June (Fig. 5b). When the ML is deep in September–November (Figs. 5c,d),

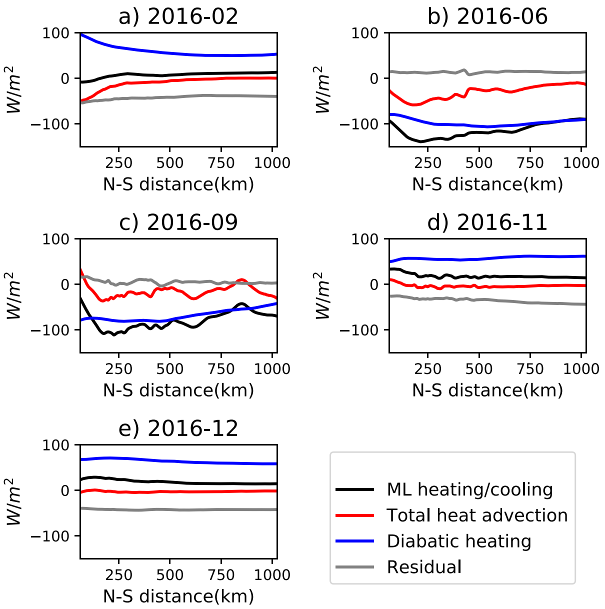

FIG. 6. Zonal-mean and monthly mean ML heat budget terms (W m^{-2}) in the WC case: ML heating/cooling term, ML heat advection term, diabatic heating term, and the residual term. The residual term includes heat diffusion at the base of the ML, lateral diffusion of heat, and numerical errors. The legend is shown at the lower-right corner. Average uncertainty, measured by standard error of the mean (SEM), in ML heating/cooling is 0.70 W m^{-2}. Average uncertainty in heat advection is 3.17 W m^{-2}. Average uncertainty in surface heat flux is 0.23 W m^{-2}. Average uncertainty in residual is 2.68 W m^{-2}.

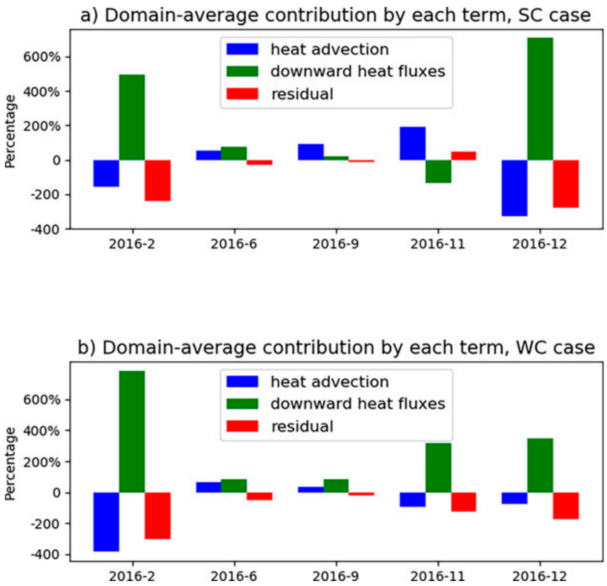

FIG. 7. Domain-average contribution of each heat budget term, divided by the ML heating/cooling term in selected months in the (a) SC case and (b) WC case. Positive (negative) values mean that the process has a warming (cooling) effect on the temperature tendency of the ML.

the advection term dominates the ML heat balance and explains most of the ML heating/cooling. Throughout most of the year, the ML heating/cooling term is nearly always in phase with the advection term. There is a strong advection term signal between 600- and 900-km distance, where the large-scale zonal currents are the strongest. In the WC case (Fig. 6), the diabatic heating term is always the largest term in the heat budget, although its relative importance decreases when ML deepens. From May to October, the ML-integrated advection term is always in phase with the ML heating/cooling term, but is smaller in magnitude compared to the diabatic heating term. There is a stronger advection signal around 200–300 km north of the southern boundary because the flow is stronger in this region of the WC domain. We can measure the uncertainties in the zonal-mean heat budget by the annual- and domain-mean standard errors of the zonal mean values. These uncertainty values are reported in the captions of Figs. 5 and 6; they are small compared to the zonal-mean values shown in Figs. 5 and 6.

Monthly and domain-average contributions by each term of the heat budget are presented in Fig. 7. Seasonal variations are fairly similar between the SC and WC cases. In summer, the downward heat flux contributes to the temperature tendency, while the heat advection and residual terms counteract the surface warming. In winter (June–September), heat advection contributes to the temperature tendency. In September for the SC case, the contribution of the advection term is much larger than the contribution by the surface heat fluxes. In contrast, advection plays a secondary role throughout the year in the WC case.

To sum up, the importance of the advection increases in winter when the ML is deeper. In the SC case, the zonal-mean ML heat budget is dominated by surface heat fluxes in summer, and by the advection in winter, especially at the jet region where ocean currents are stronger. In the WC case, the diabatic heating term is always the largest term throughout the year, although its relative importance decreases as the ML deepens. The zonal-mean budget analysis shows the dominant processes in the large-scale heat budget, and the relative importance of advection is controlled by both the ocean current speed and MLD. For the Agulhas Return Current region, Tamsitt et al. (2016) found that convergence of geostrophic and vertical temperature advection is balanced mainly by the ocean surface heat loss, with a smaller contribution from the ageostrophic advection term. This is consistent with our overall assessment of the zonal-mean heat budget in the SC case, in which surface heat fluxes dominate in summer and advection dominates in winter.

2) MESOSCALE MIXED LAYER HEAT BUDGET

Seasonal heat budget at the mesoscales is analyzed next by high-pass filtering the heat budget Eq. (4) with a 300 km × 300 km square filter, in lieu of the decomposition Eqs. (13) and (14). In both the SC (Fig. 8) and WC (Fig. 9) cases, the advection term is stronger in September than in February because of deeper ML. Unlike in the zonal-scale balance discussed in the previous section, the advection dominates the mesoscale heat balance in all seasons. In the SC case

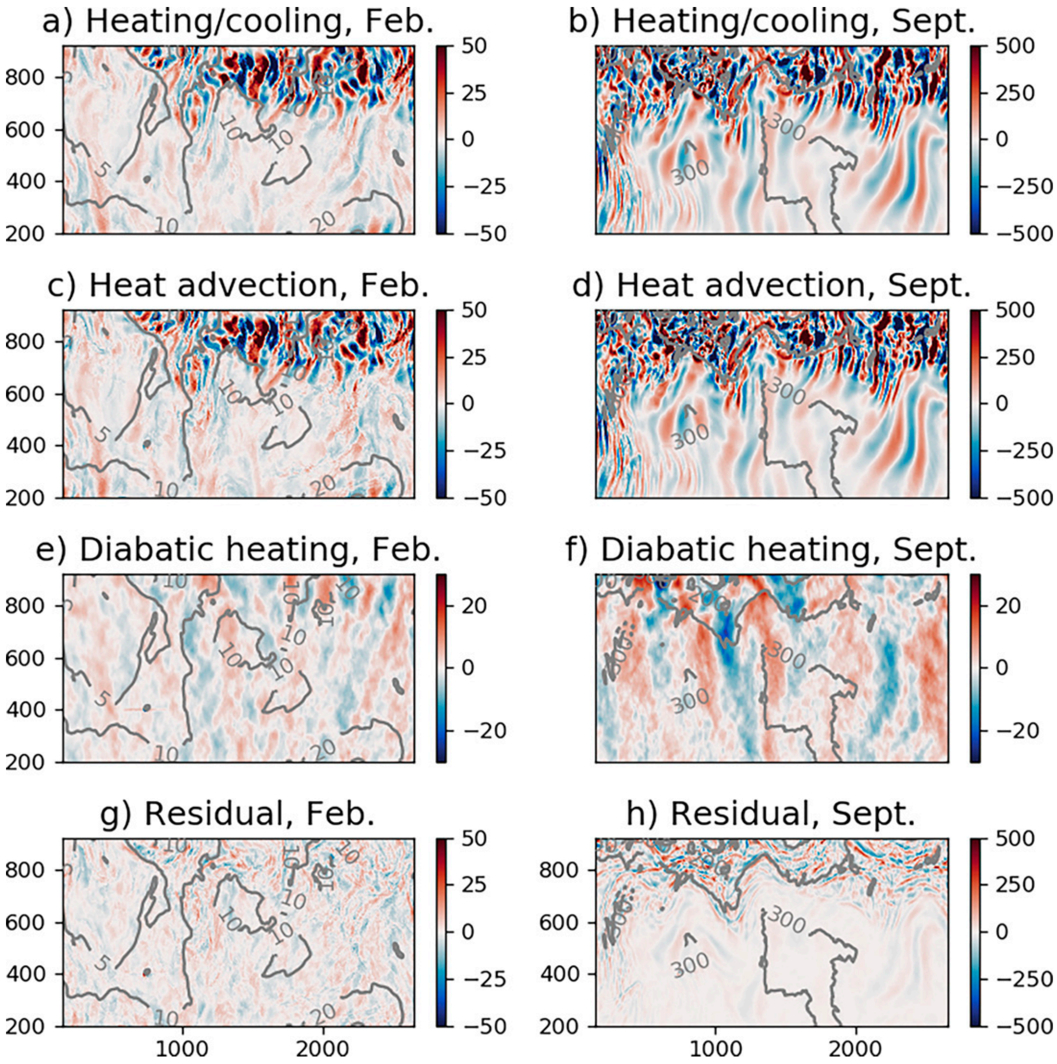

FIG. 8. High-pass-filtered ML heat budget terms (W m^{-2}) in the SC case: (a),(b) ML heating/cooling term, (c),(d) ML temperature advection term, (e),(f) ML diabatic heating term, and (g),(h) the residual term. The x axis (y axis) is west–east (north–south) distance (km).

(Fig. 8), the mesoscale heating/cooling is almost identical to the ML heat advection in both February and September, whereas other terms of the budget are smaller. In the SC case (Fig. 8), spatial Pearson correlation coefficients between ML heating/cooling and advection (Figs. 8a–d) are 0.67 and 0.69 in February and September, respectively. The spatial correlation coefficients between ML heating/cooling (Figs. 8a,b) and turbulent heat fluxes (Figs. 8e,f) are 0.19 and 0.04 in February and September, respectively. (All correlation values in this study are significant unless stated otherwise.) It is worth noting that these two terms have the shape of meridionally elongated bands, with the meridional length scale (approximately 200 km) being about twice the zonal length scale (approximately 100 km). The zonal length scale of these anomalies is smaller than the scale of the SST anomalies in Fig. 2b. Meridionally elongated modes are common features of the mesoscale fields as they correspond to the most unstable modes of the baroclinic instability (e.g., Berloff and Kamenkovich 2013). Mesoscale diabatic heating, which acts to dampen SST anomalies, has a longer zonal scale than the heating/cooling term; the residual term is negligible. In the WC case (Fig. 9), advection explains most of the heating/cooling in winter, whereas all terms play comparable roles in summer heat budget. In the WC case, the spatial Pearson correlation coefficients between ML heating/cooling and advection (Figs. 9a–d) are 0.62 and 0.39 in February and September, respectively. The correlation coefficients between ML heating/cooling (Figs. 9a–b) and turbulent heat fluxes (Figs. 9e,f) are 0.31 and 0.33 in February and September, respectively. The relative importance of the diabatic heating to the heating/cooling term increases in summer, since the heating/cooling term in the austral summer (tens of W m^{-2}) is much smaller than in the austral winter (hundreds of W m^{-2}), as shown in Figs. 8 and 9. However, correlation between diabatic

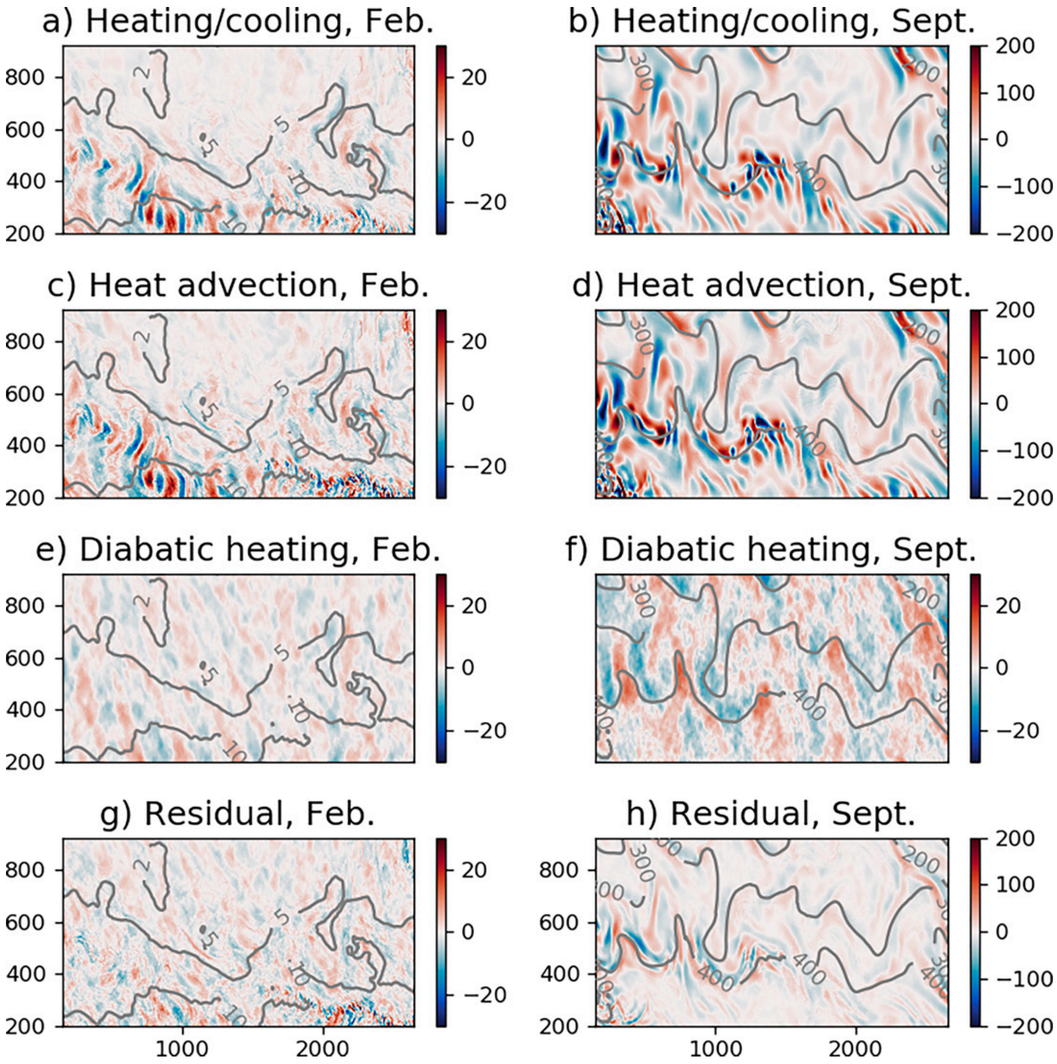

FIG. 9. High-pass-filtered ML heat budget terms (W m^{-2}) in the WC case: (a),(b) ML heating/cooling term, (c),(d) ML temperature advection term, (e),(f) ML diabatic heating term, and (g),(h) the residual term. The x axis (y axis) is west–east (north–south) distance (km).

heating and ML heating/cooling remains low. Furthermore a low correlation between the SST tendency and diabatic heating at the mesoscales is also featured in Kirtman et al. (2012), indicating that the SST tendency is not driven by the turbulent heat fluxes but is instead a result of oceanic processes.

In summary, heat advection plays an important role in the mesoscale ML heat budget and accounts for most of the spatial variability in the ML heating/cooling. The advection is particularly important in winter when the ML is deep, and in the SC case, where the currents are strong.

3) SCALING ANALYSIS

To interpret the seasonality in the relative importance of oceanic heat advection and diabatic heating, we can use scaling analysis for the main terms in the heat budget. The ratio between the corresponding terms is

$$\frac{\text{ML integrated heat advection}}{\text{diabatic heating}} = \left(-\rho_0 C_p \int_{-H}^{0} \mathbf{u}\cdot\nabla\theta\, dz\right)\Big/(Q_{\text{net}} - q), \qquad (15)$$

which can be estimated as

$$G = \frac{\rho C_p H U \delta\theta}{QL} = \frac{\rho C_p H \delta\theta}{Q\tau}, \qquad (16)$$

where L and U are the representative spatial and velocity scales, respectively; H is the MLD;

$$\tau = L/U \qquad (17)$$

is the advective time scale associated with changes in temperature due to the heat advection; and $\delta\theta$ is the change in temperature over τ. The main parameters that determine G are the strength of the advection, the MLD, and the diabatic heating. For example, stronger currents correspond to a shorter

TABLE 1. Monthly average values used in the scaling analysis.

Case name	Month	MLD avg (m)	MLD std (m)	U avg (cm s^{-1})
Strong Current (SC)	Feb 2016	11.7	5.2	4.6
	Jun 2016	132.0	34.7	4.8
	Sep 2016	310.9	47.3	4.8
	Dec 2016	11.7	5.2	5.6
Weak Current (WC)	Feb 2016	7.1	5.2	2.8
	Jun 2016	103.0	43.3	2.5
	Sep 2016	332.7	93.8	2.5
	Dec 2016	37.9	17.1	2.9

advective time scale τ and, thus, larger G, meaning that the advection is more important than diabatic heating.

We next use the parameter G to interpret the seasonality and scale dependence in the mesoscale heat budget. For these anomalies, the horizontal length scale L can be estimated to be one-fourth of the total wavelength (Phillips 1963). For the mesoscale ML heat budget, we can estimate the spatial scale L to be 60 km since this is about 1/4 of the wavelength in Fig. 2b. The velocity scale U is the monthly and spatial average surface speed, while the range of MLD is derived from the monthly average field. The monthly values of each case and month are in Table 1. Consider a temperature change of 0.5°C and turbulent heat fluxes $Q = 10$ W m^{-2}, which are typical average values for high-pass-filtered fields in both the SC and WC cases. Using these values, we can plot G in the τ–H parameter space in Fig. 10. The heat advection is always at least as important as the diabatic heating, since G is always equal to or larger than 1, in both the SC and WC cases. In winter, spring, and fall, when the MLD is deep, the role of diabatic heating is secondary to the role of the heat advection. In the summer months (December through February), when the MLD is shallow, the diabatic heating is similar in magnitude to the advection for both the SC and WC cases. The advective time scale is approximately 15 and 25 days in the SC and WC cases, respectively, because the high-pass-filtered current speed is slower in the WC case than that in the SC case. The difference in the current speed affects G in June: G is much larger in the SC case (approximately 20) than in the WC case (approximately 8). In summary, the key factors in the scale analysis are the advective time scale and the MLD. The advective time scale, which depends on the current speed (U), is shorter in the SC case than in the WC case, and the MLD is deeper in winter than in summer.

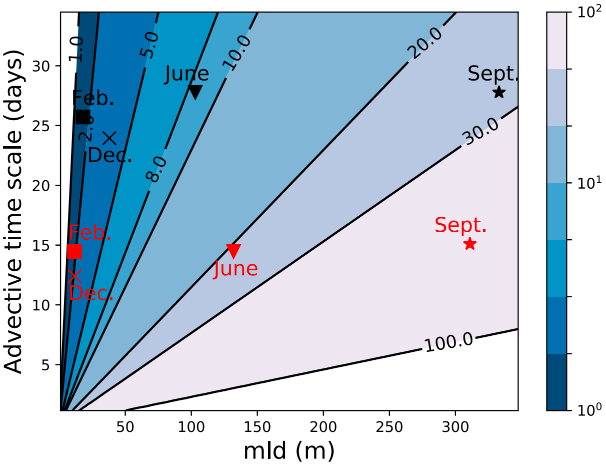

FIG. 10. The nondimensional G number that quantifies the relative importance of the ML-integrated oceanic advection, compare to the diabatic heating at mesoscale. The G number is shown as a function of the advective time scale (days) and the MLD (m). The SC (WC) case is shown by red (black) symbols.

b. Role of mesoscale heat advection

1) OCEANIC HEAT ADVECTION AND ML HEATING/COOLING

To gain further insight into the mesoscale dynamics, we analyze the relationship between various terms in Eqs. (13) and (14). We then explore the scale dependence in these relationships by analyzing the zonal and mesoscale anomalies in Eqs. (13) and (14). The relationship between various terms discussed here is quantified using binned statistics, done in the following way. First, we calculate the advection and heating/cooling terms at each grid point. Then we bin the mesoscale heat advection into 50 intervals based on its values and calculate the mean and standard deviation of the corresponding values of the ML heating/cooling in each bin. In the full budget (Fig. 11a), the total heat advection has a strong linear relationship with the ML heating/cooling, which means that the ML responds to the advective heating/cooling by oceanic currents. This relationship suggests that it is the oceanic advection that causes the temperature tendency in the heat budget, which is consistent with some previous studies (Small et al. 2020). The heat advection anomalies are similarly important in setting the zonal heating/cooling anomalies of the upper ocean (Fig. 11b), and also have a relatively strong relationship with the ML heating/cooling quantified by the Pearson correlation coefficients between the bin-average values (Table 2). The correlation coefficient is high for both the zonal and mesoscale anomalies and both the WC and SC cases, although the mesoscale field shows a lower correlation. As expected, the range of the advection values is larger in the SC case than in the WC case.

In the SC case, the relationship between the advection and ML heating/cooling is more linear in the case of zonal anomalies. This is expected, since the zonal heat advection anomalies are similar to the total heat advection, which is the

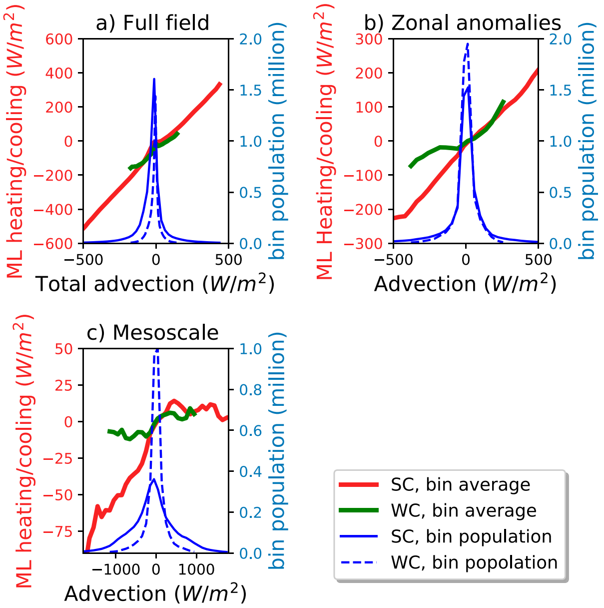

FIG. 11. Relationships between ML heating/cooling and mesoscale advection with binning based on the advection values (see text for details): (a) total ML heating/cooling and total advection, (b) zonal ML heating/cooling and zonal advection anomalies, and (c) mesoscale ML heating/cooling and mesoscale advection anomalies. The red (green) lines correspond to the SC (WC) case. The solid (dashed) blue lines show the bin population in the SC (WC) case. The average binned standard deviation of ML heating/cooling are 9.15 W m^{-2} (SC) and 56.46 W m^{-2} (WC) in (a), 188.83 W m^{-2} (SC) and 51.81 W m^{-2} (WC) in (b), and 154.29 W m^{-2} (SC) and 36.05 W m^{-2} (WC) in (c).

primary cause of the ML heating/cooling. In contrast, the relationship between the mesoscale advection and ML heating/cooling is asymmetrical (Fig. 11c). In Fig. 11c, on the left half of the plot, the ML cooling is in a nearly linear relationship with the advection in the SC case, while the ML warming is almost insensitive to the strong advective warming on the right half of the plot. The asymmetry between the warming and cooling parts of the curve is likely to be explained by the relative importance of the diabatic warming/cooling. As the air is generally cooler than the ocean in this region, atmospheric cooling of warm SST anomalies will be stronger than the warming of the cold SST anomalies. Results, therefore, suggest that the mesoscale dynamics are more complicated than the zonal-anomaly dynamics, although their effect is less significant for ML heating/cooling because of much smaller magnitudes.

The relationship between advection and ML heating/cooling is nonlinear in the WC case. For the zonal anomalies, the binned average heating/cooling is similar to that in the SC case when the advection is heating the mixed layer, while it is much weaker when the advection is cooling. The mesoscale heat advection is not correlated with the ML warming in the WC case. According to the analysis of the previous section, the diabatic heating is more important in the WC case than in the SC case (Fig. 9), breaking a strong relation between the advection and heating/cooling in the WC case.

We next calculate the coupling coefficients between bin-average ML heating/cooling and ML-integrated heat advection using a weighted linear regression model (Table 2). The coupling coefficient is the regression slope of the weighted linear regression model, which can also be interpreted as a measure of sensitivity of ML heating/cooling to advection. We also report the percentage of variance explained by the linear regression model (R^2). For the full unfiltered fields, the coupling coefficient is 0.909 (unitless) in the SC case, which means that the ML heating/cooling is strongly coupled with the advection. For the zonal anomalies, the coupling coefficient is 0.419 and 0.249 in the SC and WC cases, respectively, which means that the advection only partially explains the ML heating/cooling. For the mesoscale anomalies, the coupling coefficient is 0.038 and 0.024 in the SC and WC case, respectively, and the variance explained by the linear regression model is also relatively low (2). Therefore, we conclude that the mesoscale advection has a small direct effect on ML heating/cooling compared to full-field and zonal anomalies.

In summary, the ML heating/cooling zonal anomalies are primarily consistent with heat advection. In contrast, the relationship is significantly weaker in the case of mesoscale anomalies, and other processes, such as diabatic heating and vertical mixing, play an important role. The relationship between heating/cooling and advection is generally stronger in the SC case than in the WC case, demonstrating the importance of ocean currents' strength in the ML heat budgets.

TABLE 2. Results of the bin analysis: the ML heating/cooling and ML-integrated advection coupling coefficients, variance explained by the weighted linear regression (R^2) and Pearson correlation coefficients. The weights in the weighted least squares regression are given by the inverse of the bin variance and normalized to one. The coupling coefficients for each pair of variables are the regression slope computed from the bin-average values. Correlation coefficient is the Pearson correlation coefficient computed from the bin-average ML heating/cooling and ML-integrated advection.

Case name	Scale	Coupling coefficient	R^2	Correlation coefficient
Strong Current (SC)	Full-field	0.909	98%	0.9982
	Zonal anomalies	0.419	97%	0.9834
	Mesoscale anomalies	0.038	70%	0.8918
Weak Current (WC)	Full-field	0.658	97%	0.9835
	Zonal anomalies	0.249	93%	0.9378
	Mesoscale anomalies	0.024	82%	0.8862

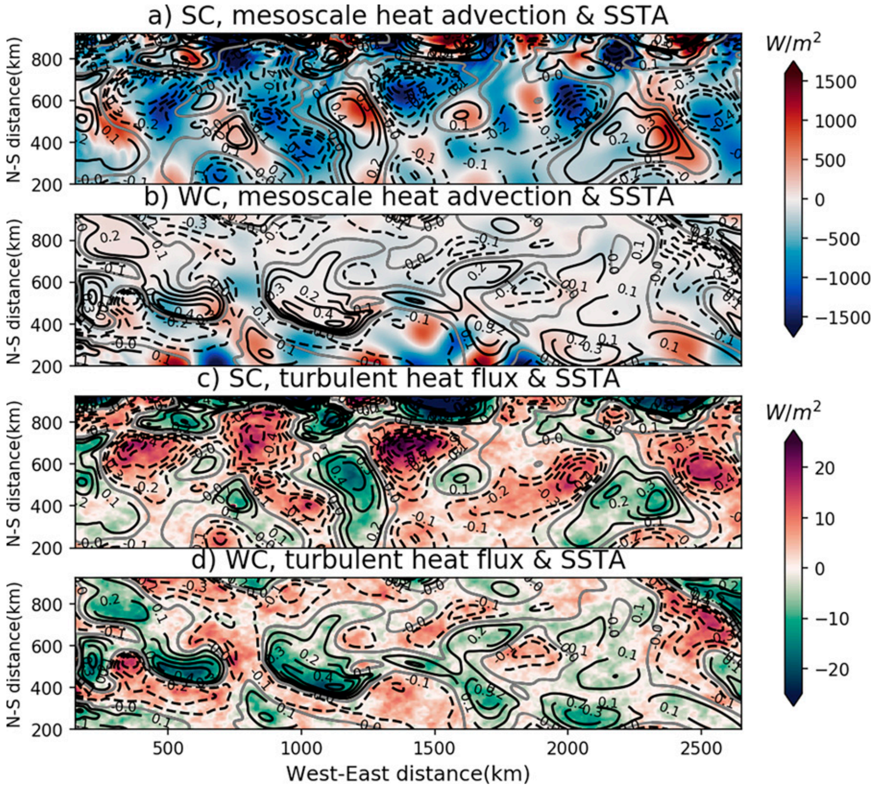

FIG. 12. Mesoscale heat advection (blue–red shading) and SST anomalies (contours) under 300-km filter in the (a) SC case and (b) WC case. Turbulent heat flux (green–magenta shading) and SST anomalies (contours) in the (c) SC case and (d) WC case. Downward heat flux (into the ocean) is positive. Positive (negative) contours are the solid (dashed) lines, and the zero contour is in gray. All fields are monthly means of August 2016. The Pearson correlation coefficient between mesoscale advection and SST anomalies is 0.35 and 0.12 in the SC and WC case, respectively.

2) OCEANIC HEAT ADVECTION AND SST ANOMALIES

One of the most important goals of this study is to establish how the mesoscale heat advection creates SST anomalies and, thus, affects the air–sea thermal coupling by inducing anomalous turbulent heat fluxes. Note that the relation between the advection and SST anomalies is not straightforward even if the advection dominates the heat budget, because the advection, in this case, controls the ML heating/cooling, but not necessarily the SST anomalies themselves. In addition, according to the decomposition of the total heat advection in Eq. (13), the variability of heat advection comes from three parts: the velocity variability, the temperature variability, and their covariability. An analysis of a coarse-resolution state estimate by Buckley et al. (2015) revealed that the temperature and velocity anomalies are negatively correlated in the geostrophic regime and, thus, the statistical link between SST anomalies and advection is far from obvious. The zonal SST anomalies are not correlated with the oceanic advection and are not shown here, despite the fact that the advection controls the ML heating/cooling. This result demonstrates that the importance of the advection in the heat budget does not guarantee that the term is directly related to SST anomalies. It may be because these large-scale SST anomalies can largely be stationary patterns. In contrast, the monthly mean mesoscale SST anomalies are weakly positively correlated with the mesoscale advection (Figs. 12a,b). The spatial correlation coefficient between two-dimensional mesoscale advection and SST anomalies in August is 0.35 and 0.12 in the SC and WC cases, respectively (Figs. 12a,b). The turbulent (latent + sensitive) heat fluxes into the ocean are strongly negatively correlated with the SST anomalies. The spatial correlation coefficient in August is −0.94 and −0.88 in the SC and WC case, respectively. The warm/cool anomalies induce upward/downward turbulent heat fluxes in both the SC and WC cases, which act to damp these SST anomalies (Figs. 12c,d). We further explore the relationship between mesoscale advection and SST anomalies using binned statistics (Table 3). The mesoscale advection–SST relationship in the SC case is stronger, as shown by the coupling coefficient. The coupling coefficient is 1.218×10^{-4} and 4.582×10^{-4} °C W^{-1} m^2 in the SC and WC case, respectively, which suggests that the SST anomalies are more sensitive to mesoscale advection in the SC case than in the WC case. The results, therefore, suggest that mesoscale SST anomalies are caused by mesoscale heat

TABLE 3. Results of the bin analysis: The coupling coefficients, variance explained by the weighted linear regression (R^2) and Pearson correlation coefficients. See Table 2 for the computation of coupling coefficients, correlation coefficients and variance explained.

Case name	Variables	Coupling coefficient	R^2	Correlation coefficient
Strong current (SC)	Mesoscale advection–SST anomalies	1.218×10^{-4} (°C W^{-1} m^2)	72%	0.837
	Mesoscale advection–turbulent heat flux	−0.0028	73%	−0.830
Weak current (WC)	Mesoscale advection–SST anomalies	4.582×10^{-5} (°C W^{-1} m^2)	76%	0.882
	Mesoscale advection–turbulent heat flux	−0.0014	76%	−0.889

advection, rather than atmospheric processes. As in the previous section, the difference between the SC and WC cases demonstrates that this relationship depends on the overall current speed.

As in the previous section, we establish an overall positive relationship between mesoscale advection and SST anomalies in the SC case, while this relationship is relatively weak in the WC case (Fig. 13a). The following discussion, therefore, focuses on the SC case only. The bin-average SST anomalies are nearly linear with the mesoscale heat advection, except for the extreme negative and positive values of advection. We can roughly identify three regimes: the extreme advective cooling regime (from −2000 to −1000 W m^{-2}), the intermediate regime (from −1000 to 1000 W m^{-2} with 95% of data) and the extreme advective warming regime (1000–2000 W m^{-2}). In the intermediate and extreme warming regimes, the slope of the curve is positive, which implies that stronger advective warming (cooling) is related to larger warm (cold) SST anomalies. The slope steepens in the extreme warming regime, which indicates an increased sensitivity of SST anomalies to advection. However, in the extreme cooling regime, we observe an inverse relationship between the two variables, implying that stronger advective cooling is increasingly less effective in inducing cold SST anomalies. The nonlinearity can be attributed to variations in MLD (Fig. 13c). In the extreme cooling regime, the ML deepens because of destratification at the base of the ML caused by cooling. The deepening leads to larger heat inertia making the effects of the ML heat advection less effective in controlling the SST anomalies. This negative feedback explains why increasingly strong advective cooling does not necessarily cause stronger cold SST anomalies. In the extreme warming regime, the advective warming leads to more stable stratification, shallower ML, and decreased thermal inertia. This is positive feedback: the more intense the warming is, the easier it is to warm the SST. The positive feedback can explain a greater rate of change in the extreme warming regime than in the intermediate regime. To support this hypothesis, we analyzed variations in MLD and verified that ML deepens with the cooling mesoscale advection and vice versa. The Pearson correlation coefficient between the bin-average ML tendency and mesoscale heat advection is −0.912. A separate study will address the mesoscale MLD variability in the Southern Ocean.

Since the turbulent heat flux damps the SST anomalies, we also find a strong relationship between the mesoscale advection and air–sea heat fluxes (Fig. 13b). The bin-averaged turbulent heat fluxes are negatively correlated with the advection, as shown in Table 3. The coupling coefficient is −0.0028 and −0.0014 in the SC and WC case, respectively, which shows that the coupling strength is about twice as strong in the SC than that in the WC case. This is the first study that directly links the oceanic advection and air–sea heat exchanges at the oceanic mesoscale. This advection–SST–heat flux relationship is results from the ocean-driven mesoscale air–sea coupling in the Southern Ocean.

To assess the robustness of our conclusions from the heat budget analysis, we have also tried different time averaging periods: 10 days, 20 days, 1 month, 2 months, and 3 months for both mesoscale and zonal anomalies. The same conclusions still hold true. For the mesoscale anomalies, the 1-month average yields the best correlation between SST anomalies and mesoscale advection, while 10- and 20-day averages show lower correlation. For the zonal anomalies, the correlation remains low for all averaging periods.

In summary, the mesoscale heat advection has a strong and nearly linear relationship with SST anomalies in the SC case. In contrast, SST anomalies in the WC case are less sensitive to the mesoscale heat advection. The causation of SST anomalies can also be established by eliminating such processes as diabatic heating and vertical diffusion, which both damp SST anomalies. The nearly linear relationship depends on the strength of the currents, as illustrated by the differences between the SC and WC cases. The relationship is further modulated by MLD, with a deepening (shoaling) ML increasing (decreasing) the thermal inertia and weakening (enhancing) the SST–advection–heat flux relation.

c. Role of Ekman heat advection

The heat advection is an important term in the ML heat budget, especially in winter when the ML is deep. The heat advection term is composed of two parts: the Ekman advection that is locally forced by the wind, and the geostrophic and ageostrophic processes (intrinsic oceanic variability), which exhibit strong mesoscale variability. The ageostrophic variability is expected to be much weaker than geostrophic part since the Rossby numbers in both SC and WC domain are much smaller than 1. The Ekman heat transport is expected to play a role in regions with strong wind variability and SST gradients. Similar to Small et al. (2020), the Ekman heat advection can be estimated as

$$Q_{\text{Ekman}} = \frac{C_p}{f}\left(\tau_x \frac{\delta \text{SST}}{\delta y} - \tau_y \frac{\delta \text{SST}}{\delta x}\right), \tag{18}$$

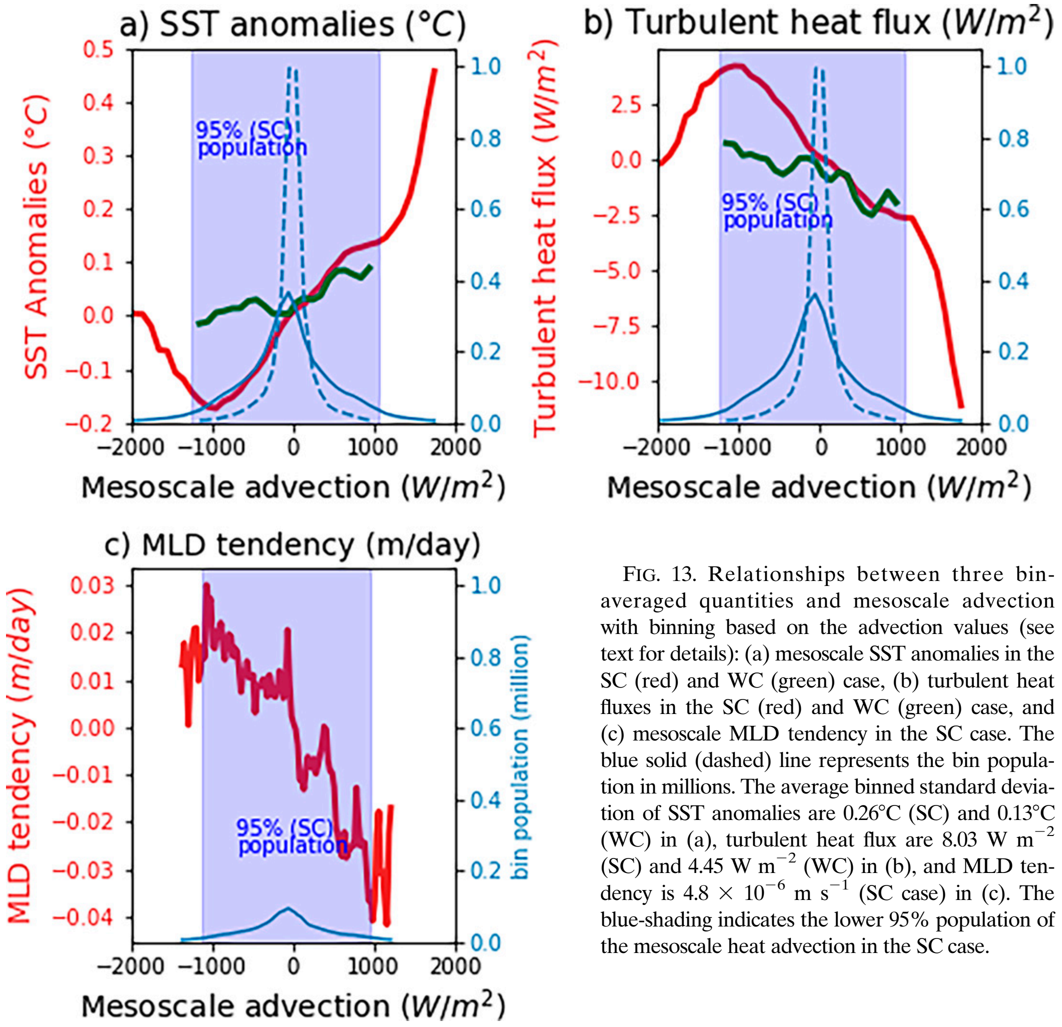

FIG. 13. Relationships between three bin-averaged quantities and mesoscale advection with binning based on the advection values (see text for details): (a) mesoscale SST anomalies in the SC (red) and WC (green) case, (b) turbulent heat fluxes in the SC (red) and WC (green) case, and (c) mesoscale MLD tendency in the SC case. The blue solid (dashed) line represents the bin population in millions. The average binned standard deviation of SST anomalies are 0.26°C (SC) and 0.13°C (WC) in (a), turbulent heat flux are 8.03 W m^{-2} (SC) and 4.45 W m^{-2} (WC) in (b), and MLD tendency is 4.8×10^{-6} m s^{-1} (SC case) in (c). The blue-shading indicates the lower 95% population of the mesoscale heat advection in the SC case.

where the temperature in the Ekman layer is assumed to be equal to the SST. In this study, we decompose the total heat advection into Ekman advection and intrinsic oceanic advection, with the intrinsic oceanic advection defined as the difference between the total advection and Q_{Ekman}. We find the relative importance of Ekman and intrinsic oceanic advection is modulated by the MLD, with the role of Ekman advection being secondary to the intrinsic oceanic advection when MLD is deep. In winter (Fig. 14), spring and fall, when the ML is deep, the ML heating/cooling is primarily caused by the intrinsic ocean variability. In summer (Fig. 15), when the ML is the shallowest, the ML heating/cooling is caused by both Ekman advection and intrinsic ocean variability. Besides, the mesoscale wind stress is also stronger in winter than in summer, which further contributes to the seasonal variations. These results hold true for both the SC and WC cases and can be compared with previous studies by Buckley et al. (2015), Tamsitt et al. (2016), and Small et al. (2020). Similar to our conclusions about the winter balance, Small et al. (2020) concluded that the Ekman advection plays a secondary role in the heat budget compared to the geostrophic heat advection in the western boundary regions and ACC, which means that the SST variability comes mainly from intrinsic ocean dynamics instead of atmospheric forcing in these regions with strong currents. Buckley et al. (2015) made a similar conclusion about the Gulf Stream region. Tamsitt et al. (2016) also found that, in the Agulhas Return Current region, the ageostrophic advection plays a smaller role than the geostrophic advection and surface heat fluxes. Our study, however, found that the Ekman heat advection is as important as the intrinsic ocean variability in summer. These previous studies considered heat budgets over a fixed depth and did not account for variations in MLD, which explains the difference with our analysis and outlines the importance of MLD variations. For example, Small et al. (2020) analyzed the heat budget of the upper 50 and 400 m, while the MLD in ROAM simulations is mostly less than 50 m in summer.

Another distinct feature of the summertime heat budget is the tendency of the Ekman heat advection to compensate for the geostrophic and ageostrophic advection. Because most of the mesoscale wind anomalies are induced by the SST anomalies in our study (Perlin et al. 2020), this compensation can be interpreted as the negative feedback of the winds to

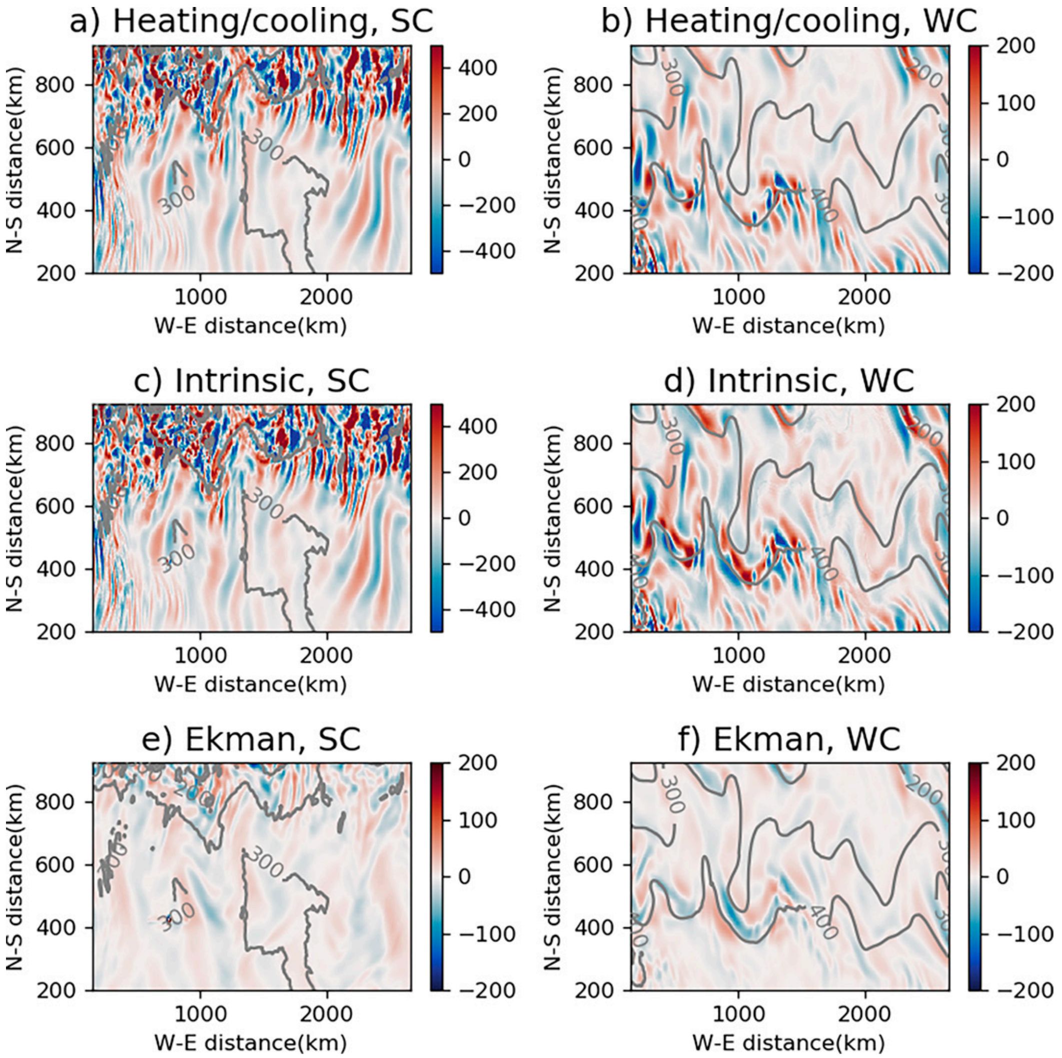

FIG. 14. Relative importance of the geostrophic and Ekman advection in winter, in the (left) SC and (right) WC cases: (a),(b) ML heating/cooling, (c),(d) ML-integrated intrinsic ocean advection (geostrophic and ageostrophic heat advection; W m^{-2}), and (e),(f) Ekman heat advection (W m^{-2}). All fields are monthly mean of September 2016.

the intrinsic SST variability. Seo et al. (2016) concluded that SST-induced Ekman pumping can be significant enough to affect propagation of mesoscale eddies in the California Current System. Note, however, that the depth of the Ekman layer is comparable to the shallow summertime MLD in parts of our domain, which complicates the quantitative comparison of the Ekman advection and ML-integrated geostrophic and ageostrophic advection. That said, our overall assessment of the Ekman heat advection is mostly consistent with Small et al. (2020) in the Southern Ocean: Ekman advection plays a secondary part in most of the year, while the intrinsic oceanic variability is what causes the heating and cooling of the upper ocean.

4. Summary and conclusions

This numerical study focuses on the role of mesoscale currents in the ML heat budget and air–sea thermal coupling. The semi-idealized numerical simulations are carried out in two different settings: the SC case with overall faster ocean currents, stronger meridional temperature gradient and higher eddy kinetic energy (EKE), and the WC case with slower ocean currents, smaller meridional temperature gradient and weaker mesoscale variability. We found that the relationship between mesoscale heat advection and SST variability is determined by the ocean current strength and variations in MLD. At mesoscale, the ML heat advection is the primary process that sustains SST anomalies in the regions with strong currents. These anomalies, in turn, induce an atmospheric response with thermal damping, and our results demonstrate a nearly linear relationship between the advection and turbulent surface fluxes in the SC case. This relationship is significantly weaker in the WC case. Because the mesoscale anomalies are defined with an explicit spatial scale, they are most relevant to the eddies that are missing

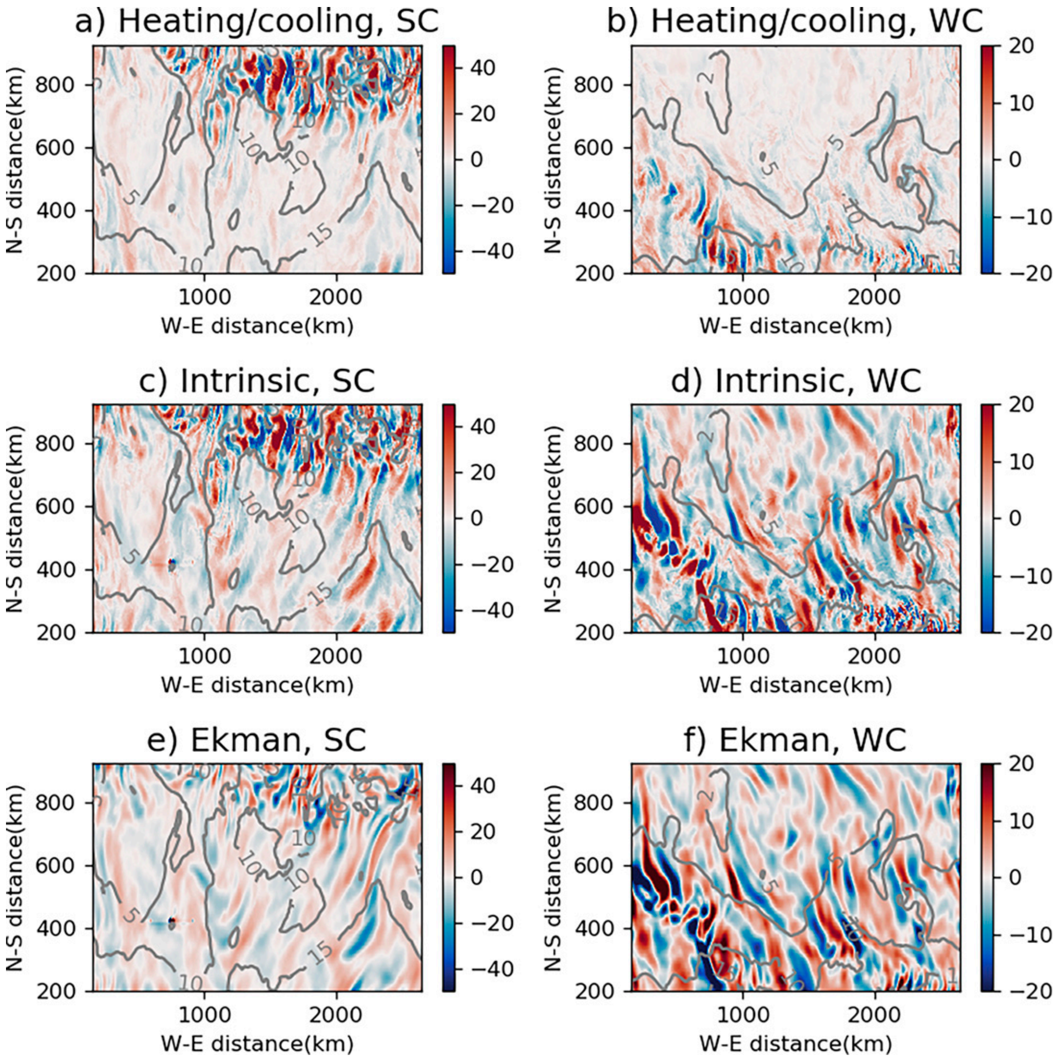

FIG. 15. Relative importance of the geostrophic and Ekman advection in summer, in the (left) SC and (right) WC cases: (a),(b) ML heating/cooling, (c),(d) ML-integrated intrinsic ocean advection (geostrophic and ageostrophic heat advection; W m^{-2}), and (e),(f) Ekman heat advection (W m^{-2}). All fields are monthly mean of February 2016.

in the standard (coarser) resolution models. The situation is different for zonal anomalies. Although the zonal heat advection anomalies are important in the ML heating/cooling, the relationship between the SST anomalies and heat advection is not observed. This is likely to be explained by the fact that the zonal SST anomalies largely consist of nearly stationary meanders and correspond to a local balance between advection and diabatic heating/cooling. Despite the importance of advection in the overall heat budget, the actual relationship between the advection and SST can, therefore, be expected to be weaker than in the case of transient mesoscale SST anomalies.

The importance of MLD revealed by this study extends beyond the thermal inertia, which modulates the effectiveness of the surface heating/cooling in Tozuka and Cronin (2014) and Tozuka et al. (2018). In our study, MLD also modulates the dominance of the lateral heat advection, which controls the ML heat budget wherever the ML is deep. For example, the zonal-mean heat budget shows strong seasonality, mainly due to drastic seasonal variability in the MLD. In the SC case, the advection dominates the ML heat balance in winter, while the diabatic heating term dominates in summer. In the WC case, the relative importance of the advection increases in winter, however, the diabatic heating term remains the biggest term throughout the year. The relative importance of the residual term in the budget is larger in summer than in winter, which is explained by tighter stratification and stronger diffusion in summer. The scale analysis further confirms that the mesoscale heat advection is more important than the diabatic surface heating, except in summer when MLD is very shallow.

As another manifestation of the importance of MLD, the role of the Ekman heat advection is shown to be secondary to intrinsic ocean variability in explaining mesoscale heating/

cooling, except in summer when the ML is shallow. Therefore, intrinsic ocean variability, rather than the wind forcing and diabatic heating, is the most important process in the ML heat budget and mesoscale SST variability. This assessment of the relative importance of the mesoscale Ekman advection is consistent with the conclusion of Small et al. (2020) in the Southern Ocean. Although the localized Ekman advection acts to reduce the SST variance in the Southern Ocean (Larson et al. 2018), its overall effect on mesoscale SST variability is not as significant as the effect of the intrinsic ocean variability.

The idealized setting of the ocean component, with the same topography in both the SC and WC cases, simplifies a direct comparison between the two regimes with different currents. The conclusions and scale analysis from this study can be expected to be sufficiently generic and applicable to other regions of the ocean. When interpreting the conclusions from this study, we should keep in mind several sources of biases and uncertainties: 1) The 2-yr segment of the atmospheric forcing (used to force the atmospheric model) does not represent the entire range of atmospheric conditions, although we can reasonably expect our conclusions to be qualitatively the same for other time periods. 2) The model is a semi-idealized reentrant channel model that is designed to mimic two distinct flow regimes, and it cannot represent the complete dynamics of the real Southern Ocean. 3) The comparison between wind-driven Ekman advection and intrinsic ocean variability has the caveat that the depth of the Ekman layer could be different from the MLD. Specific conclusions from our semi-idealized simulations will need validation with observations. Subsurface sampling of the ocean at short spatial scales are, however, costly, which raises the value of model-based studies.

Acknowledgments. This study is supported by the National Science Foundation (NSF) Research Awards 1559151 and 1849990. We thank the University of Miami's Center of Computational Science for providing computing resources. We also acknowledge the high-performance computing support from Cheyenne provided by NCAR's Computational and Information Systems Laboratory, sponsored by NSF. We thank the editors and three anonymous reviewers for their helpful comments and constructive criticism. We also thank Dr. Arthur Mariano for his recommendations of statistical analysis techniques.

Data availability statement. The original data of the numerical simulations used in the study are too large to archive or to transfer. Instead, we provide the aggregated monthly average data and the information necessary to replicate and analyze the simulations. The description of the model and simulations can be found in Perlin et al. (2020). The aggregated data and the Python codes used for the analysis are shared in this data repository: https://doi.org/10.17604/94qh-6m66.

REFERENCES

Berloff, P., and I. Kamenkovich, 2013: On spectral analysis of mesoscale eddies. Part II: Nonlinear analysis. *J. Phys. Oceanogr.*, **43**, 2528–2544, https://doi.org/10.1175/JPO-D-12-0233.1.

Bishop, S. P., R. J. Small, F. O. Bryan, and R. A. Tomas, 2017: Scale dependence of midlatitude air–sea interaction. *J. Climate*, **30**, 8207–8221, https://doi.org/10.1175/JCLI-D-17-0159.1.

——, ——, and ——, 2020: The global sink of available potential energy by mesoscale air-sea interaction. *J. Adv. Model. Earth Syst.*, **12**, e2020MS002118, https://doi.org/10.1029/2020MS002118.

Buckley, M. W., R. M. Ponte, G. Forget, and P. Heimbach, 2014: Low-frequency SST and upper-ocean heat content variability in the North Atlantic. *J. Climate*, **27**, 4996–5018, https://doi.org/10.1175/JCLI-D-13-00316.1.

——, ——, ——, and ——, 2015: Determining the origins of advective heat transport convergence variability in the North Atlantic. *J. Climate*, **28**, 3943–3956, https://doi.org/10.1175/JCLI-D-14-00579.1.

Chelton, D. B., R. A. Deszoeke, M. G. Schlax, K. E. Naggar, and N. Siwertz, 1998: Geographical variability of the first baroclinic Rossby radius of deformation. *J. Phys. Oceanogr.*, **28**, 433–460, https://doi.org/10.1175/1520-0485(1998)028<0433:GVOTFB>2.0.CO;2.

Cronin, M. F., and Coauthors, 2013: Formation and erosion of the seasonal thermocline in the kuroshio extension recirculation gyre. *Deep-Sea Res. II*, **85**, 62–74, https://doi.org/10.1016/j.dsr2.2012.07.018.

Dong, S., S. T. Gille, and J. Sprintall, 2007: An assessment of the Southern Ocean mixed layer heat budget. *J. Climate*, **20**, 4425–4442, https://doi.org/10.1175/JCLI4259.1.

——, J. Sprintall, S. T. Gille, and L. Talley, 2008: Southern Ocean mixed-layer depth from Argo float profiles. *J. Geophys. Res.*, **113**, C06013, https://doi.org/10.1029/2006JC004051.

Faure, V., M. Arhan, S. Speich, and S. Gladyshev, 2011: Heat budget of the surface mixed layer south of Africa. *Ocean Dyn.*, **61**, 1441–1458, https://doi.org/10.1007/s10236-011-0444-1.

Hodur, R. M., 1997: The Naval Research Laboratory's Coupled Ocean/Atmosphere Mesoscale Prediction System (COAMPS). *Mon. Wea. Rev.*, **125**, 1414–1430, https://doi.org/10.1175/1520-0493(1997)125<1414:TNRLSC>2.0.CO;2.

Kirtman, B. P., and Coauthors, 2012: Impact of ocean model resolution on CCSM climate simulations. *Climate Dyn.*, **39**, 1303–1328, https://doi.org/10.1007/s00382-012-1500-3.

Larson, S. M., D. J. Vimont, A. C. Clement, and B. P. Kirtman, 2018: How momentum coupling affects SST variance and large-scale Pacific climate variability in CESM. *J. Climate*, **31**, 2927–2944, https://doi.org/10.1175/JCLI-D-17-0645.1.

Laurindo, L. C., L. Siqueira, A. J. Mariano, and B. P. Kirtman, 2019: Cross-spectral analysis of the SST/10-m wind speed coupling resolved by satellite products and climate model simulations. *Climate Dyn.*, **52**, 5071–5098, https://doi.org/10.1007/s00382-018-4434-6.

Li, Q., and S. Lee, 2017: A mechanism of mixed layer formation in the Indo–Western Pacific Southern Ocean: Preconditioning by an eddy-driven jet-scale overturning circulation. *J. Phys. Oceanogr.*, **47**, 2755–2772, https://doi.org/10.1175/JPO-D-17-0006.1.

Liu, W. T., A. Zhang, and J. K. B. Bishop, 1994: Evaporation and solar irradiance as regulators of sea surface temperature in annual and interannual changes. *J. Geophys. Res.*, **99**, 12623, https://doi.org/10.1029/94JC00604.

Ma, X., and Coauthors, 2016: Western boundary currents regulated by interaction between ocean eddies and the atmosphere. *Nature*, **535**, 533–537, https://doi.org/10.1038/nature18640.

Mazloff, M. R., P. Heimbach, and C. Wunsch, 2010: An eddy-permitting Southern Ocean state estimate. *J. Phys. Oceanogr.*, **40**, 880–899, https://doi.org/10.1175/2009JPO4236.1.

Okumura, Y., S.-P. Xie, A. Numaguti, and Y. Tanimoto, 2001: Tropical Atlantic air-sea interaction and its influence on the NAO. *Geophys. Res. Lett.*, **28**, 1507–1510, https://doi.org/10.1029/2000GL012565.

O'Neill, L. W., D. B. Chelton, and S. K. Esbensen, 2012: Covariability of surface wind and stress responses to sea surface temperature fronts. *J. Climate*, **25**, 5916–5942, https://doi.org/10.1175/JCLI-D-11-00230.1.

Orsi, A. H., T. Whitworth, and W. D. Nowlin, 1995: On the meridional extent and fronts of the Antarctic Circumpolar Current. *Deep-Sea Res. I*, **42**, 641–673, https://doi.org/10.1016/0967-0637(95)00021-W.

Paulson, C., and J. Simpson, 1977: Irridiance measurements in the upper ocean. *J. Phys. Oceanogr.*, **7**, 952–956, https://doi.org/10.1175/1520-0485(1977)007<0952:IMITUO>2.0.CO;2.

Pennel, R., and I. Kamenkovich, 2014: On the factors controlling the eddy-induced transport in the Antarctic circumpolar current. *J. Phys. Oceanogr.*, **44**, 2127–2138, https://doi.org/10.1175/JPO-D-13-0256.1.

Perlin, N., S. P. de Szoeke, D. B. Chelton, R. M. Samelson, E. D. Skyllingstad, and L. W. O'Neill, 2014: Modeling the atmospheric boundary layer wind response to mesoscale sea surface temperature perturbations. *Mon. Wea. Rev.*, **142**, 4284–4307, https://doi.org/10.1175/MWR-D-13-00332.1.

——, I. Kamenkovich, Y. Gao, and B. P. Kirtman, 2020: A study of mesoscale air–sea interaction in the Southern Ocean with a regional coupled model. *Ocean Modell.*, **153**, 101660, https://doi.org/10.1016/j.ocemod.2020.101660.

Phillips, N. A., 1963: Geostrophic motion. *Rev. Geophys.*, **1**, 123–176, https://doi.org/10.1029/RG001i002p00123.

Putrasahan, D. A., I. Kamenkovich, M. Le Hénaff, and B. P. Kirtman, 2017: Importance of ocean mesoscale variability for air-sea interactions in the Gulf of Mexico: Ocean mesoscale air-sea processes in GoM. *Geophys. Res. Lett.*, **44**, 6352–6362, https://doi.org/10.1002/2017GL072884.

Reynolds, R. W., T. M. Smith, C. Liu, D. B. Chelton, K. S. Casey, and M. G. Schlax, 2007: Daily high-resolution-blended analyses for sea surface temperature. *J. Climate*, **20**, 5473–5496, https://doi.org/10.1175/2007JCLI1824.1.

Roberts, C. D., M. D. Palmer, R. P. Allan, D. Desbruyeres, P. Hyder, C. Liu, and D. Smith, 2017: Surface flux and ocean heat transport convergence contributions to seasonal and interannual variations of ocean heat content. *J. Geophys. Res. Oceans*, **122**, 726–744, https://doi.org/10.1002/2016JC012278.

Sallée, J.-B., N. Wienders, K. Speer, and R. Morrow, 2006: Formation of subantarctic mode water in the southeastern Indian Ocean. *Ocean Dyn.*, **56**, 525–542, https://doi.org/10.1007/s10236-005-0054-x.

——, K. Speer, R. Morrow, and R. Lumpkin, 2008: An estimate of Lagrangian eddy statistics and diffusion in the mixed layer of the Southern Ocean. *J. Mar. Res.*, **66**, 441–463, https://doi.org/10.1357/002224008787157458.

——, K. G. Speer, and S. R. Rintoul, 2010: Zonally asymmetric response of the Southern Ocean mixed-layer depth to the Southern Annular Mode. *Nat. Geosci.*, **3**, 273–279, https://doi.org/10.1038/ngeo812.

Seo, H., A. J. Miller, and J. R. Norris, 2016: Eddy–wind interaction in the California current system: Dynamics and impacts. *J. Phys. Oceanogr.*, **46**, 439–459, https://doi.org/10.1175/JPO-D-15-0086.1.

Shchepetkin, A. F., and J. C. McWilliams, 2005: The Regional Oceanic Modeling System (ROMS): A split-explicit, free-surface, topography-following-coordinate oceanic model. *Ocean Modell.*, **9**, 347–404, https://doi.org/10.1016/j.ocemod.2004.08.002.

Small, R. J., and Coauthors, 2008: Air–sea interaction over ocean fronts and eddies. *Dyn. Atmos. Oceans*, **45**, 274–319, https://doi.org/10.1016/j.dynatmoce.2008.01.001.

——, F. O. Bryan, S. P. Bishop, and R. A. Tomas, 2019: Air–sea turbulent heat fluxes in climate models and observational analyses: What drives their variability? *J. Climate*, **32**, 2397–2421, https://doi.org/10.1175/JCLI-D-18-0576.1.

——, ——, ——, S. Larson, and R. A. Tomas, 2020: What drives upper-ocean temperature variability in coupled climate models and observations? *J. Climate*, **33**, 577–596, https://doi.org/10.1175/JCLI-D-19-0295.1.

Tamsitt, V., L. D. Talley, M. R. Mazloff, and I. Cerovečki, 2016: Zonal variations in the Southern Ocean heat budget. *J. Climate*, **29**, 6563–6579, https://doi.org/10.1175/JCLI-D-15-0630.1.

Tozuka, T., and M. F. Cronin, 2014: Role of mixed layer depth in surface frontogenesis: The Agulhas Return Current front. *Geophys. Res. Lett.*, **41**, 2447–2453, https://doi.org/10.1002/2014GL059624.

——, S. Ohishi, and M. F. Cronin, 2018: A metric for surface heat flux effect on horizontal sea surface temperature gradients. *Climate Dyn.*, **51**, 547–561, https://doi.org/10.1007/s00382-017-3940-2.

Vallis, G. K., 2006: *Atmospheric and Oceanic Fluid Dynamics.* Cambridge University Press, 745 pp.

Vivier, F., D. Iudicone, F. Busdraghi, and Y.-H. Park, 2010: Dynamics of sea-surface temperature anomalies in the Southern Ocean diagnosed from a 2D mixed-layer model. *Climate Dyn.*, **34**, 153–184, https://doi.org/10.1007/s00382-009-0724-3.